Article

Coupling the Piezoelectric Effect and the Plasmonic Effect to Enhance the Photocatalytic Degradation of Ciprofloxacin in Au-Ferroelectric $Bi_4Ti_3O_{12}$ Nanofibers

Chao Meng [1,2], Junfeng Peng [3], Lei Wang [1], Hao Han [1,*], Kai Yang [4,*] and Daotong You [3,*]

1 State Key Laboratory of NBC Protection for Civilian, Beijing 102205, China
2 School of Materials Design & Engineering, Beijing Institute of Fashion Technology, Beijing 100029, China
3 School of Chemistry and Chemical Engineering, Jiangxi University of Science and Technology, Ganzhou 341000, China
4 Institute of Photonics Technology, Jinan University, Guangzhou 511443, China
* Correspondence: thinkinghh@163.com (H.H.); yangkai@jxust.edu.cn (K.Y.); ydtseu@126.com (D.Y.)

Abstract: In this study, ferroelectric $Bi_4Ti_3O_{12}$ and $Au-Bi_4Ti_3O_{12}$ nanofibers were synthesized by electrospinning and ion sputtering. The piezoelectric effect of $Bi_4Ti_3O_{12}$ and the surface plasmon effect of Au were used to improve the photogenerated electron–hole separation and optical absorption. The results of the characterization showed successful preparation of the orthorhombic $Bi_4Ti_3O_{12}$ nanofibers, in which the absorption band edge was 426 nm with a 2.91 eV band gap. The piezo-photocatalytic activity of the $Bi_4Ti_3O_{12}$ was tested through the degradation of the antibiotic ciprofloxacin under three different experimental conditions: light, vibration, and light plus vibration. All of the ciprofloxacin was degraded after 80 min in piezo-photocatalytic conditions, with a piezo-photocatalytic degradation rate of 0.03141 min^{-1}, which is 1.56 and 3.88 times, respectively, that of photocatalysis and piezo-catalysis. After loading Au on the $Bi_4Ti_3O_{12}$, the degradation efficiency was improved under all three conditions, and the piezoelectric photocatalytic efficiency of $Au-Bi_4Ti_3O_{12}$ for ciprofloxacin degradation was able to reach 100% in 60 min with a piezo-photocatalytic degradation rate of 0.06157 min^{-1}. The results of the photocurrent and impedance tests indicated that the photocurrent density of $Bi_4Ti_3O_{12}$ nanofibers loaded with Au is increased from 5.08×10^{-7} A/cm^2 to 8.17×10^{-6} A/cm^2, which is 16.08 times higher than without loading the Au. This work provides an effective way to improve the conversion efficiency of photocatalysis to degrade organic pollutants by combining the plasmon effect and the piezoelectric effect.

Keywords: photocatalysis; environmental applications; antibiotic ciprofloxacin; piezoelectric effect

1. Introduction

According to research, China is the world's largest producer and user of antibiotics. However, the abuse of antibiotics can make some pathogenic bacteria resistant, and their long-term survival in the environment would be a threat to human health and the security of the ecological environment. Avoiding the abuse of antibiotics and the degradation of antibiotics in rivers has become our research focus. Ciprofloxacin (CIP) is the third generation of synthetic quinolone antibacterial drugs, which have broad-spectrum antibacterial activity and good bactericidal effects [1,2]. It is widely used in animal husbandry to prevent and treat diseases. However, CIP is widely exposed to water ecosystems, and even at very low concentrations, it can cause a serious threat to human and ecological environments. Traditional physical separation technology, biological methods and other water treatment technologies cannot effectively remove these antibiotics [3,4]. Therefore, it is a challenge to develop effective and environment-friendly technologies for degrading antibiotics [5]. The emergence of photocatalytic technologies has brought hope to this urgent problem due to their environment-friendly nature and cost effectiveness [6,7]. Photocatalysis mainly

involves the following processes: (1) a semiconductor is excited by photons with an energy greater than its band gap in order to generate electrons and holes [8–10]; (2) photogenerated electrons and holes are separated and migrated to the surface effectively [11–14]; (3) a surface redox reaction occurs to degrade the antibiotics [15–17]. However, for common semiconductor photocatalysts, the photogenerated electrons and holes are prone to recombination during the migration process and cannot generate highly reactive radicals. As a result, the catalytic activity and efficiency of the photocatalyst are greatly reduced.

Over the last few years, the piezoelectric polarization-based method known as piezocatalysis has undergone rapid improvement in the domain of environmental mitigation and production of fuels [18–20]. On the application of mechanical force, the polarization of a piezoelectric semiconductor takes place, leading to the accumulation of oppositely charged localized polarizations on opposite surfaces. Consequently, the free charge carriers (electrons and holes) are separated after being driven through the built-in piezoelectric field, thereby allowing their participation in the surface redox reactions. Up to now, many piezoelectric materials have been demonstrated to be promising for application in the piezo-phototronic degradation of environmental pollutants [21–23]. However, a large proportion of piezoelectrical materials have poor electrical conductivity, which seriously restricts the transport of the charge carriers across the interface formed with other active materials.

$Bi_4Ti_3O_{12}$ has a unique, layered structure with perovskite-like $(Bi_2Ti_3O_{10})^{2-}$ units alternating with $(Bi_2O_2)^{2+}$ layers [24]. The $(Bi_2O_2)^{2+}$ layers contain many oxygen vacancies, which can expand the wavelength range of light absorption. In addition, $(Bi_2O_2)^{2+}$ and $(Bi_2Ti_3O_{10})^{2-}$ layers can form an inner electrical field [25], which could promote the separation of photo-generated electrons and holes. Its unique crystal and electronic structures endow $Bi_4Ti_3O_{12}$ with excellent ferroelectricity and piezoelectricity, fatigue resistance and a high Curie temperature. Therefore, $Bi_4Ti_3O_{12}$ can be used as an ideal material for piezo-phototronic degradation of organic pollutants.

It is generally accepted that the performance of different materials depends highly on their morphologies and microstructures [26,27]. $Bi_4Ti_3O_{12}$ nanofibers have large specific surface areas, high porosity, small volumes, light weights, good flexibility and bending properties. The piezoelectric properties of continuous-filament nanofibers are better than those of granular and blocky ones. Moreover, the introduction of a noble metal, such as gold (Au), on the surface of $Bi_4Ti_3O_{12}$ can not only help improve the absorbing efficiency of the light, but also enhance the separation efficiency of photogenerated electrons and holes due to the resonant oscillation of the surface plasmon effect [28,29].

In order to solve the problem of CIP release and to avoid rapid recombination between the electrons and holes of $Bi_4Ti_3O_{12}$, we synthesized $Bi_4Ti_3O_{12}$ nanofibers using the electrospinning method and then investigated the catalytic degradation of ciprofloxacin under different conditions to verify the photocatalytic properties of $Bi_4Ti_3O_{12}$ nanofibers. To enhance the photocatalytic activity in the degradation of the substrate and explore the internal mechanism of photocatalysis, Au-$Bi_4Ti_3O_{12}$ material was prepared. The results show that the catalytic effect and light absorption were all enhanced due to the local surface plasmon effect after loading Au on the $Bi_4Ti_3O_{12}$, which is of great significance for improving the photocatalytic effects and studying the mechanism of the degradation. This work introduces the synergistic effects of SPR and piezotronic effects to promote the separation of electron–hole pairs and improve the piezo-photocatalytic degradation of ciprofloxacin using Au-$Bi_4Ti_3O_{12}$ nanofiber heterostructures, which offer an efficient technology to design high-performance catalysts for environmental purification.

2. Results and Discussion

2.1. Characterization of the Morphology

The SEM images of $Bi_4Ti_3O_{12}$ nanofibers before calcining and after calcining are shown in Figure 1. The SEM image of the dried $Bi_4Ti_3O_{12}$ precursor without calcination after electrospinning shows that the nanofibers are interlaced (Figure 1a), which indicates that the electrospinning was in good condition. The SEM image presented in Figure 1b shows

that the $Bi_4Ti_3O_{12}$ still maintains a fibrous structure after calcining, which indicates that only the PVP was removed, and the structure of the $Bi_4Ti_3O_{12}$ nanofibers was not affected by calcining. However, when the PVP was removed in the calcination process, the surface of the $Bi_4Ti_3O_{12}$ was no longer smooth and became a porous nanofiber structure with a diameter of about 60–80 nm.
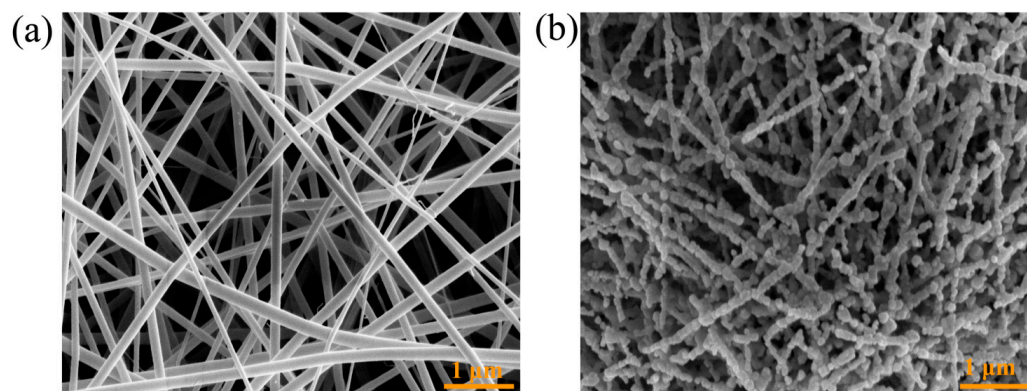

Figure 1. Scanning electron microscopy (SEM) images of $Bi_4Ti_3O_{12}$ nanofibers (**a**) before calcination and (**b**) after calcination.

The TEM and HRTEM images were measured to further investigate the microstructure of the $Bi_4Ti_3O_{12}$ nanofibers and the Au-$Bi_4Ti_3O_{12}$ nanofibers. The low-magnification TEM image of the $Bi_4Ti_3O_{12}$ shows nanofibers inlaid with particles (Figure 2a). Meanwhile, the TEM image of the Au-$Bi_4Ti_3O_{12}$ (Figure 2b) shows that the nanofibers are made up of many Au particles, with sizes ranging from 5 to 15 nm. The HRTEM image (Figure 2c) shows a lattice spacing of 0.233 nm, corresponding to the (111) planes of Au and proving that the Au nanoparticles were successfully embedded in the $Bi_4Ti_3O_{12}$ nanofiber [30].
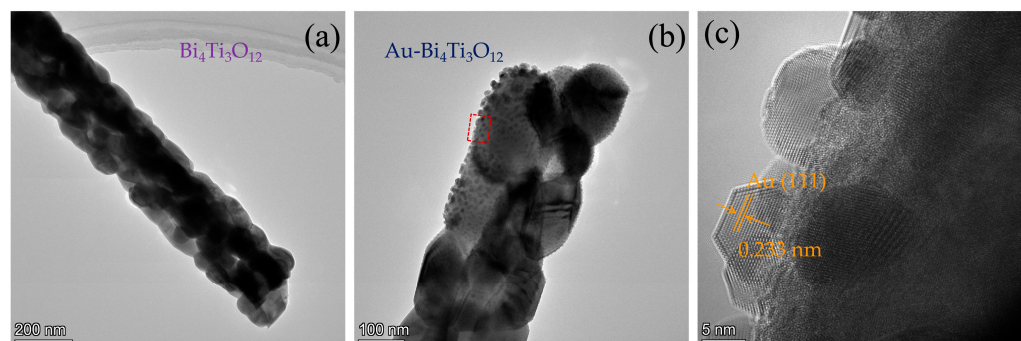

Figure 2. Transmission electron microscopy (TEM) images of (**a**) $Bi_4Ti_3O_{12}$ nanofibers and (**b**) Au-$Bi_4Ti_3O_{12}$ nanofibers, and (**c**) high-resolution TEM images of Au-$Bi_4Ti_3O_{12}$ nanofibers.

2.2. Characterization of the Crystal Structure

The phase structures of the $Bi_4Ti_3O_{12}$ nanofibers and the Au-$Bi_4Ti_3O_{12}$ nanofibers were studied using X-ray diffraction. As shown in Figure 3a, all of the diffraction peaks of the $Bi_4Ti_3O_{12}$ and Au-$Bi_4Ti_3O_{12}$ nanofibers were in accord with the standards of the database card. The characteristic peaks located at 2θ equaled 23.0°, 29.9° and 32.7° and corresponded to crystal planes (111), (117) and (020), respectively. The peak shapes demonstrated that the prepared sample had good crystallinity. Other diffraction peaks were located at 21.35°, 38.1°, 39.7°, 47.0°, 51.35°, 53.13°, 56.8° and 62.2° corresponded to crystal facets (008), (0014), (208), (202), (262), (0214), (137) and (2214), respectively. These were all part of the orthorhombic crystalline phase of $Bi_4Ti_3O_{12}$ (JCPDS 72-1019) [24]. The orthogonal crystal $Bi_4Ti_3O_{12}$ was described by the general formula of $(Bi_2O_2)^{2+}(Bi_2Ti_3O_{10})^{2-}$, which is composed of three layers of TiO_6 octahedron and $(Bi_2O_2)^{2+}$ monolayers that are alternately

stacked, so that its structure cannot be easily changed. The average crystallite size of $Bi_4Ti_3O_{12}$ was calculated by using the modified Scherer method [31]:

$$\ln\beta = \ln\left(\frac{k\lambda}{D_{SM} \cdot \cos\theta}\right) \tag{1}$$

where D_{SM} is the average crystallite size, k is a constant (equal to 0.9), β is the line broadening in radians (FWHM), θ is the Bragg angle and λ is the X-ray wavelength ($\lambda = 0.1546$ nm). The calculated crystallite size value was 18.53 nm. No typical diffraction peaks of Au were detected in the Au-$Bi_4Ti_3O_{12}$. This is because the amount of Au was too small (less than 5%) and could not be detected by the X-ray diffraction.
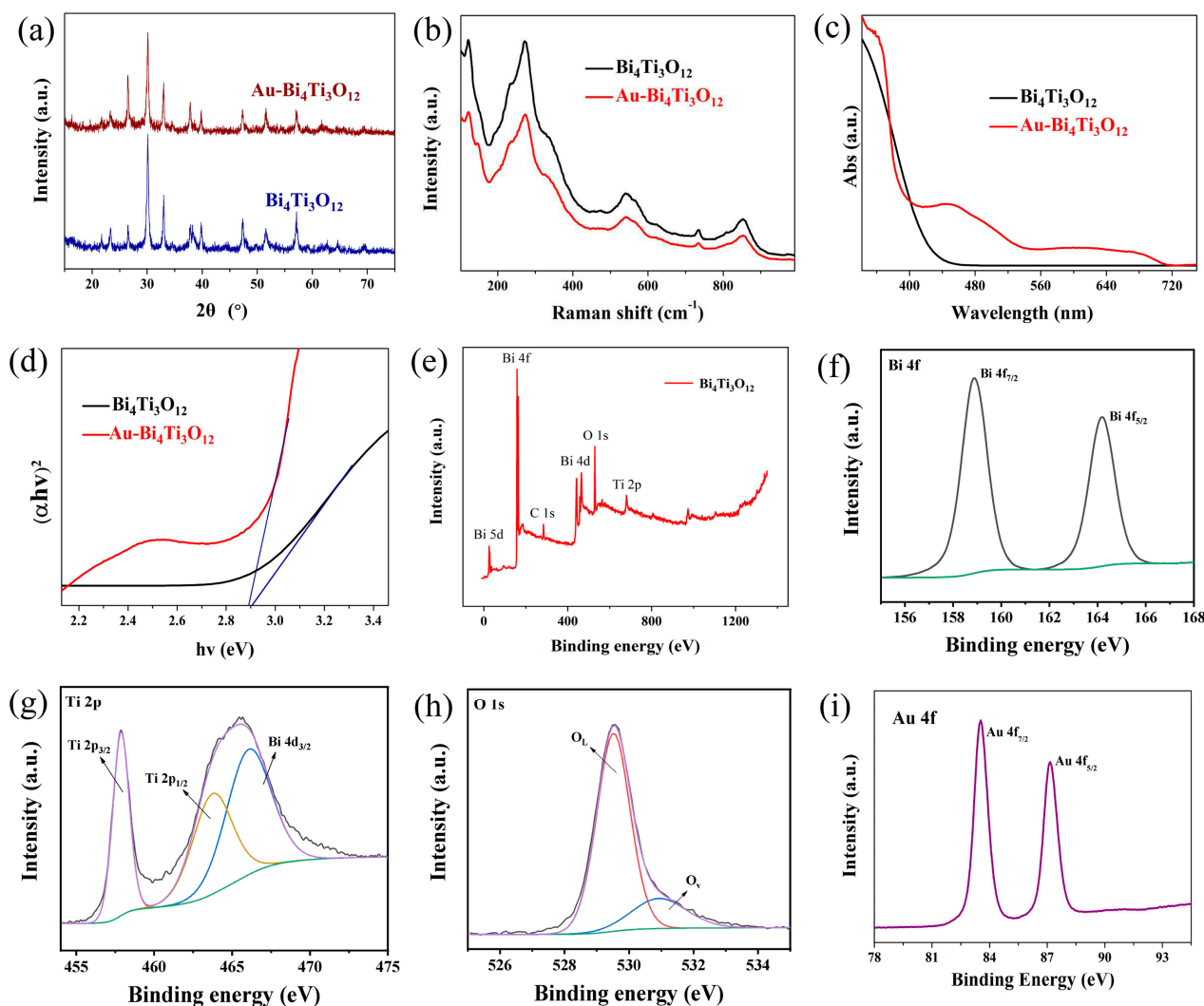

Figure 3. (**a**) X-Ray Diffraction, (**b**) Raman spectra, (**c**) UV-Vis diffuse reflectance spectra, and (**d**) A plot of the $(\alpha h\nu)^2$ versus the $h\nu$ of $Bi_4Ti_3O_{12}$ and Au–$Bi_4Ti_3O_{12}$; (**e**) X-ray photoelectron spectroscopy and high-resolution XPS spectra of (**f**) Bi 4f, (**g**) Ti 2p and (**h**) O 1s core levels of $Bi_4Ti_3O_{12}$; and (**i**) High-resolution XPS spectrum of Au 4f in Au–$Bi_4Ti_3O_{12}$.

Raman spectra of the $Bi_4Ti_3O_{12}$ and Au-$Bi_4Ti_3O_{12}$ nanofibers are shown in Figure 3b, which illustrates that the $Bi_4Ti_3O_{12}$ nanocrystals have strong phonon modes near the Raman frequency peaks of 58, 89,118, 267, 472, 537 and 846 cm^{-1}. When we compared the distribution of the $Bi_4Ti_3O_{12}$, the phonon modes corresponded to the peaks on the left or right of 200 cm^{-1}, as the boundaries were different. Low-frequency modes of less than 200 cm^{-1} were related to the vibration of Bi^{3+} and $(Bi_2O_2)^{2+}$ layers with large masses,

and high-frequency modes larger than 200 cm^{-1} were related to internal vibrations or distortions of Ti^{4+} and TiO_6 octahedra with relatively small masses. The Raman peaks at 267, 472, 537 and 846 cm^{-1} were attributed to the internal vibration modes of the TiO_6 octahedron. The peak at 267 cm^{-1} was associated with the torsional vibration mode of the TiO_6 octahedron. In accordance with the Raman rule, only the octahedral distortion was active, and the corresponding positions of peaks at 472 and 537 cm^{-1} depended on O-Ti-O bending and stretching vibrations, while the phonon mode at 846 cm^{-1} reflected the internal vibration of the octahedra and the stretching vibration of O-Ti-O. The strong and sharp mode at 55 cm^{-1} was a rigid layer mode, which originated from the layer motion, similar to the rigid-unit crystal in the layered structure [24]. The appearance of a TiO_6 octahedron vibration mode and a rigid layer mode indicated that a layered perovskite structure had formed in the prepared $Bi_4Ti_3O_{12}$ nanocrystals, which is consistent with the XRD characterization results. Au deposition on the $Bi_4Ti_3O_{12}$ surface did not change the crystalline structures of the bare $Bi_4Ti_3O_{12}$, since the spectra were similar to $Bi_4Ti_3O_{12}$.

2.3. Characterization of the Optical Properties

In this study, UV-Vis absorbance spectra were measured to clarify the optical properties of the $Bi_4Ti_3O_{12}$ nanofibers and the Au-$Bi_4Ti_3O_{12}$ nanofibers. The UV-Vis diffuse reflection absorption spectrum showed an absorption edge of 426 nm of $Bi_4Ti_3O_{12}$ (Figure 3c), which indicated that the $Bi_4Ti_3O_{12}$ had a visible light absorption capacity. Based on the equation of $Eg = 1240/\lambda$, the band gap value were able to be obtained [32], and the band gaps of the samples were estimated to be 2.91 and 2.89 eV for the $Bi_4Ti_3O_{12}$ and the Au-$Bi_4Ti_3O_{12}$, respectively (Figure 3d). However, an absorption peak was observed at around 500–600 nm after loading Au nanoparticles onto the $Bi_4Ti_3O_{12}$ nanofibers. This is attributed to the surface plasmon resonance (SPR) excitation of the Au, where the hot electrons on the surface of the Au oscillated together and resonated with incidental light, thus increasing the electromagnetic field at the vicinity of the Au surface [33].

The chemical states of the elements in $Bi_4Ti_3O_{12}$ nanofibers were analyzed using X-ray photoelectron spectroscopy (XPS) survey scan spectra, as shown in Figure 3e. The results showed that the $Bi_4Ti_3O_{12}$ nanofibers were mainly composed of Bi, Ti and O. Figure 3f shows the XPS spectrum of Bi 4f, which contains two isolated peaks at the binding energies of 158.88 eV and 164.18 eV, ascribing to Bi $4f_{7/2}$ and Bi $4f_{5/2}$, respectively. Thus, the element Bi can be ascribed to Bi^{3+} [34]. The peaks at 457.88 and 463.88 eV correspond to the binding energies of Ti $2p_{3/2}$ and Ti $2p_{1/2}$, respectively (Figure 3g), suggesting that Ti exists in the form of Ti^{4+} [24]. Figure 3h shows the high-resolution XPS spectrum of O 1s. The binding energies of O 1s at 529.48 and 530.98 eV correspond to the binding energy of the Bi-O bond and the surface hydroxyl oxygen, respectively [35,36]. The high-resolution XPS spectrum of the Au 4f in Au-$Bi_4Ti_3O_{12}$ presents two peaks at 83.0 and 86.6 eV, which are assigned to metallic Au $4f_{7/2}$ and Au $4f_{5/2}$, respectively (Figure 3i) [37].

2.4. Degradation of Ciprofloxacin

$Bi_4Ti_3O_{12}$ nanofibers and Au-$Bi_4Ti_3O_{12}$ nanofibers were used to study the photo-catalytic degradation of the ciprofloxacin antibiotic under three different experimental conditions: light, vibration, and light plus vibration. The photocatalytic performance of $Bi_4Ti_3O_{12}$ nanofibers for the degradation of CIP under Xenon lamp illumination is presented in Figure 4a. According to the results of the ultraviolet visible spectrophotometer, as the photocatalytic reaction proceeded, the main extinction peak of CIP at 270 nm and the wider peak from 300–350 nm decreased with time, which means that the CIP was effectively degraded by the light. However, there was still some CIP that was not degraded 90 min into the reaction. When the Xenon lamp illumination was replaced with vibration, the main extinction peak of CIP and the wider peak were also decreased as the reaction proceeded, but the peak decreased more slowly than in the photocatalytic condition during the same 90-min time interval (Figure 4b). By using both Xenon lamp illumination and vibration, the

CIP was almost completely degraded in 80 min (Figure 4c), which confirms our original hypothesis that piezo-photocatalytic degradation is better than either type alone.
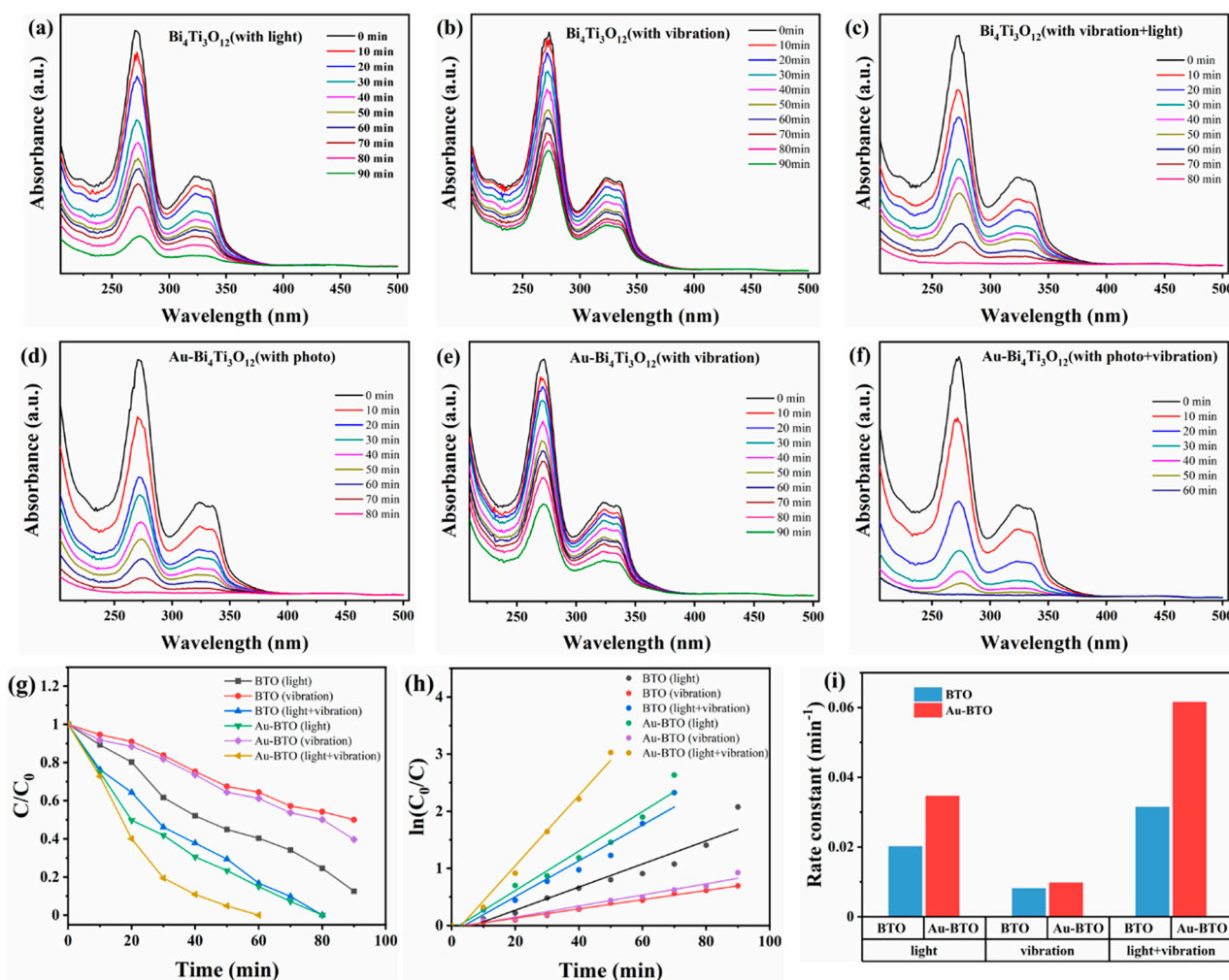

Figure 4. Absorbance spectra of the decomposition activity of ciprofloxacin with 10 min intervals under the following condition: $Bi_4Ti_3O_{12}$ (**a**) under the light, (**b**) with vibration, and (**c**) with vibration and under the light; Au–$Bi_4Ti_3O_{12}$ (**d**) under the light, (**e**) with vibration, and (**f**) with vibration and under the light; (**g**) comparison of the degradation proficiency in various test conditions; (**h**) sample kinetics fit to the information; and (**i**) comparison of the rate constant (k) values for the decomposition activity of ciprofloxacin under different conditions.

The above results prove that the degradation performance of ferroelectric $Bi_4Ti_3O_{12}$ is significantly enhanced under ultrasonic conditions, which may be ascribed to the piezoelectric effect that promotes the generation of free electrons on the surface of a piezo-catalyst. $Bi_4Ti_3O_{12}$ has ferroelectric properties and can spontaneously polarize to generate an internal electric field. Vibration pressurization of $Bi_4Ti_3O_{12}$ nanofibers can enhance the polarization electric field and light absorption. Under the enhanced polarization electric field, more photogenerated electrons and holes quickly move to both sides separately and combine with corresponding ions to the active sites of the surface. Both of these factors can enhance the catalytic effect.

When Au-$Bi_4Ti_3O_{12}$ was substituted for $Bi_4Ti_3O_{12}$, the efficiency of the degradation of CIP was increased under Xenon lamp illumination, with vibration, and with both Xenon lamp illumination and vibration (Figure 4d–f). The photocatalytic degradation trend of CIP by Au-$Bi_4Ti_3O_{12}$ was similar to that of $Bi_4Ti_3O_{12}$, but the degradation efficiency was able to reach 100% in 80 min. Moreover, by using both Xenon lamp illumination and vibration, the

piezo-photocatalytic degradation efficiency of CIP by Au-Bi$_4$Ti$_3$O$_{12}$ reached 100% just in 60 min.

For the purposes of comparison, chemical kinetics experiments were carried out for the degradation of CIP by Bi$_4$Ti$_3$O$_{12}$ and Au-Bi$_4$Ti$_3$O$_{12}$. Figure 4g displays a plot of C/C$_0$ in the degradation of CIP vs. time using Bi$_4$Ti$_3$O$_{12}$ and Au-Bi$_4$Ti$_3$O$_{12}$ under different conditions. This graph demonstrates that the concentration ratio of the CIP decreased with respect to the time period. Based on the graph of C/C$_0$ vs. time, a plot was drawn to demonstrate ln(C/C$_0$) vs. time (Figure 4h). Using this plot, we calculated the reaction rate constants (k) for the degradation efficiencies of the CIP solution by Bi$_4$Ti$_3$O$_{12}$ and Au-Bi$_4$Ti$_3$O$_{12}$ nanofibers under Xenon lamp illumination, with vibration, and with both Xenon lamp illumination and vibration conditions, as shown in Figure 4i. Based on this figure, the degradation efficiencies of CIP by Au-Bi$_4$Ti$_3$O$_{12}$ nanofibers are higher than those of the Bi$_4$Ti$_3$O$_{12}$ nanofibers under Xenon lamp illumination, with vibration, and with both Xenon lamp illumination and vibration. The degradation efficiency of the CIP solution by Au-Bi$_4$Ti$_3$O$_{12}$ nanofibers reached 100% within 60 min, with a peak reaction rate of 0.06187 min^{-1} under simultaneous light and ultrasonic vibration, which is twice as high as the peak reaction rate of the Bi$_4$Ti$_3$O$_{12}$ nanofibers. This suggests that the introduction of Au on the surface of Bi$_4$Ti$_3$O$_{12}$ can enhance the performance of Bi$_4$Ti$_3$O$_{12}$ due to the piezo-plasmonic coupling effect.

Control experiments showed that no obvious self-decolorization was observed (Figure 5a) in the absence of catalyst under light irradiation with ultrasonic excitation. To understand the mechanism of the photocatalytic reaction process, a series of comparative tests were conducted by employing holes and radical trapping agents for the degradation of ciprofloxacin. The results shown in Figure 5b. It is clear that the ciprofloxacin degradation was barely influenced with the addition of isopropanol (IPA) (as a quencher of •OH) [38]. However, after adding benzoquinone (BQ) (as a quencher of •O$_2$) and ethylenediaminetetraacetic acid disodium (EDTA-2Na) (as a quencher of h$^+$) into the reactions, the degradation rate of the ciprofloxacin was reduced significantly. The results indicate that the •O$_2$ and the photogenerated holes were the major active species participating in the photocatalytic reaction process. After light irradiation, the electron and hole appeared and separated to the surface of the Au-Bi$_4$Ti$_3$O$_{12}$ catalyst. Then the adsorbed oxygen combined with the electron and became the reactive species of superoxide radicals. With their strong oxidative ability, the •O$_2$ and holes directly oxidized the pollutants.
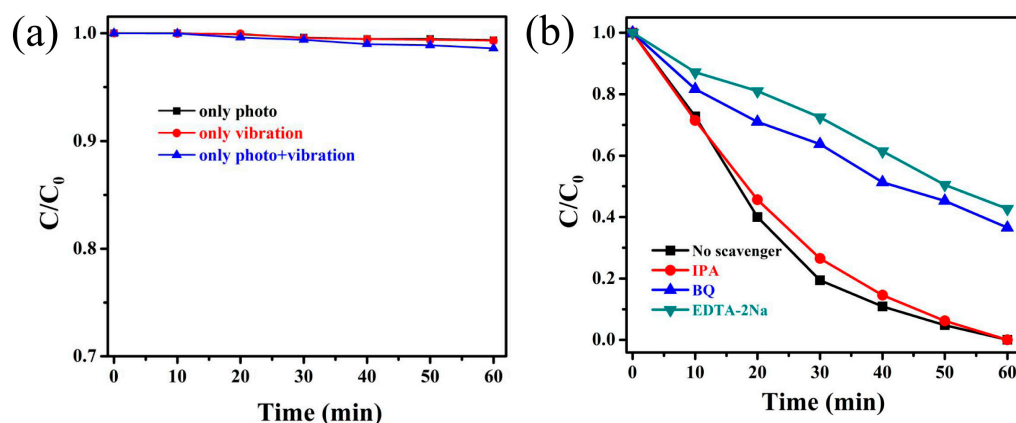

Figure 5. (**a**) Control experiments without catalyst under light irradiation with ultrasonic excitation. (**b**) Photodegradation curves of ciprofloxacin over Au-Bi$_4$Ti$_3$O$_{12}$ with different scavengers.

2.5. Photoelectrochemical Measurement

Electrochemical impedance spectroscopy (EIS) was used to understand the direction and resistance of the charge transfer [39]. The diameter of the semicircle in the figure represents the charge transfer resistance. The smaller the diameter of the semicircle is, the smaller the transfer resistance of the photo electrode is, and the higher the charge

transfer efficiency is. As shown from left to right in Figure 6, the impedance diagrams were drawn of $Bi_4Ti_3O_{12}$ nanofibers and $Au-Bi_4Ti_3O_{12}$ nanofibers under light and dark. It was found that the impedance of $Bi_4Ti_3O_{12}$ nanofibers without Au was large, and the change of additive optical impedance was very small, which indicates that the $Bi_4Ti_3O_{12}$ nanofibers were insensitive to light absorption, whereas the impedance of $Au-Bi_4Ti_3O_{12}$ nanofibers material became noticeably smaller under the light.
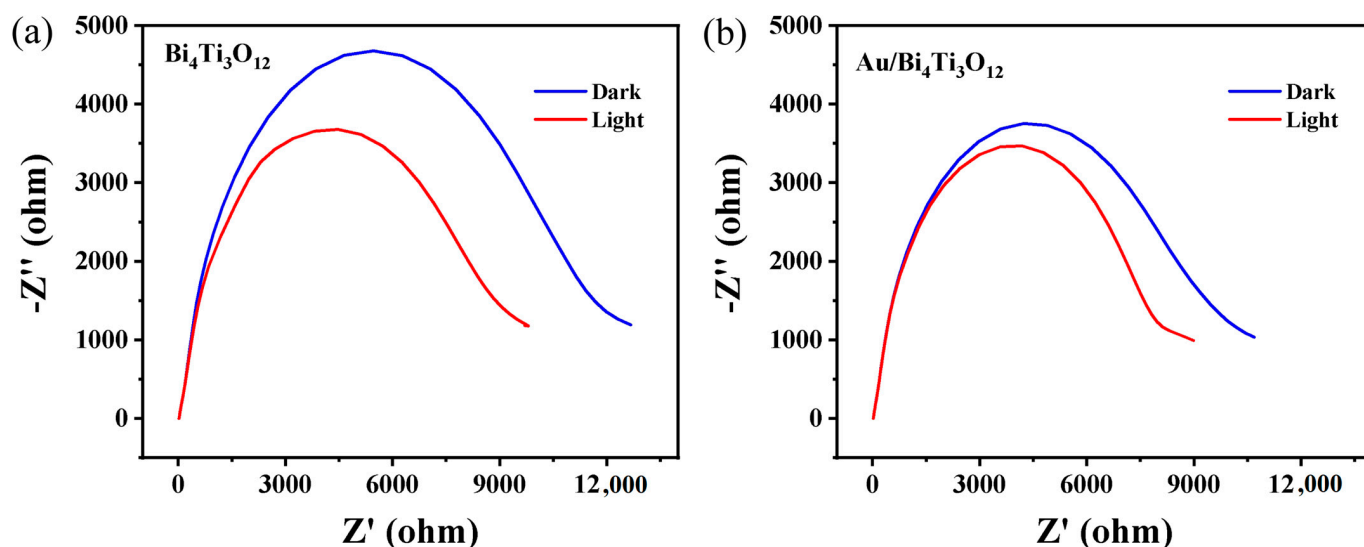

Figure 6. Electrochemical impedance spectroscopy of (**a**) $Bi_4Ti_3O_{12}$ and (**b**) $Au-Bi_4Ti_3O_{12}$ under light and dark.

Subsequently, transient photocurrent response measurements were conducted to study the separation behaviors of the photoexcited carriers during the photoreactions. As shown in Figure 7, there was generation of photocurrents with good reproducibility for both the $Bi_4Ti_3O_{12}$ and the $Au-Bi_4Ti_3O_{12}$ nanofibers. The $Bi_4Ti_3O_{12}$ nanofibers and the $Au-Bi_4Ti_3O_{12}$ nanofibers were characterized at 0 V and 0.1 V, respectively. At the same time, the photocurrent density of $Bi_4Ti_3O_{12}$ nanofibers at 0 V was 2.89×10^{-7} A/cm^2. When the voltage was changed to 0.1 V, the photocurrent density increased to 5.04×10^{-7} A/cm^2. The photocurrent density of $Au-Bi_4Ti_3O_{12}$ nanofibers at 0 V was 2.74×10^{-6} A/cm^2, and the photocurrent density at 0.1 V was 7.54×10^{-6} A/cm^2.
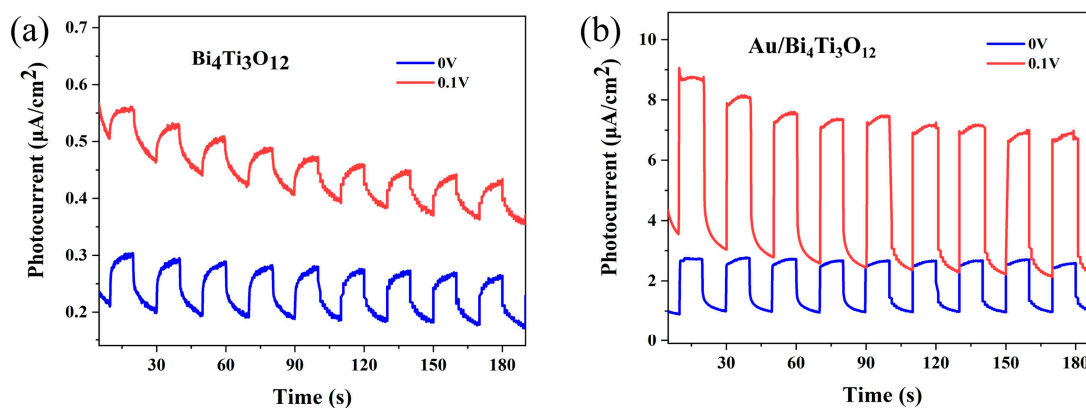
Figure 7. Photocurrent response of (**a**) $Bi_4Ti_3O_{12}$ and (**b**) $Au-Bi_4Ti_3O_{12}$ under lamp irradiation at 0 V and 0.1 V.

The current-time curve is the observation of the change of the current with time under different voltage conditions. The fact that the I-T result was consistent under EIS indicates

that loaded Au can enhance the photocatalytic performance of $Bi_4Ti_3O_{12}$ nanofibers. After absorbing light, the Au nanoparticles are excited by the light to generate hot electrons. Because of the Fermi levels generated on the contact surfaces of the Au nanoparticles and the $Bi_4Ti_3O_{12}$ nanofibers, the electrons in the Au nanoparticles move to the conduction band of the $Bi_4Ti_3O_{12}$ nanofibers [40]. At the same time, the $Bi_4Ti_3O_{12}$ nanofibers can absorb light to generate electron–hole pairs. Under the action of the polarization field, more electrons and holes are generated through transfer. On the other hand, after the local surface plasmon is excited, a large scattering cross section will be produced, and the generated hot electrons will then travel through the semiconductor and participate in the photocatalytic reaction process. Thus, loading Au can not only enhance the light absorption capacity, but also promote the separation of electrons and holes by participating in the reaction, which can explain why the introduction of Au enhances the photocatalytic performance.

3. Experimental Section

3.1. Synthesis of Bi$_4$Ti$_3$O$_{12}$ Nanofibers

First, 0.75 g of $Bi(NO_3) \cdot 5H_2O$ was poured into a bottle, and then 8 mL of N, N-dimethylformamide (DMF); 2 mL of glacial acetic acid; and 0.4 mL tetrabutyl titanate (TBT) were added into the bottle and continuously stirred for about 2 h. Subsequently, 1.25 g PVP was added into the premixed solution and stirred for about 8 h to form a precursor solution. Then the precursor solution was transferred into a 10 mL needle tube, followed by adjusting the high voltage to 18 V and the low voltage to -2 V and pushing the speed to 0.1 mm/min, with a rotation speed of 50 r/min. Then the solution was stripped and calcined in a tube furnace at 550 °C for 2 h (heating rate: 3 °C min^{-1}). After naturally cooling to room temperature, the product was washed and dried to obtain the sample $Bi_4Ti_3O_{12}$ nanofibers.

3.2. Synthesis of Au-Bi$_4$Ti$_3$O$_{12}$ Nanofibers

First, the Au was plated with a small ion sputtering instrument to obtain Au-loaded $Bi_4Ti_3O_{12}$ nanofibers. The relevant parameters were a current of 30 mA and an air pressure of 5×10^{-2} mbar/Pa that was maintained in the cavity, along with a gold plating time of 20 s.

3.3. Material Characterization

The diffraction patterns of the samples and the pellets were collected with the Rigaku D/Max 3 C X-ray diffraction (XRD) system equipped with a Cu Kα tube (wavelength = 0.154 nm) and operated at 40 kV/40 mA. The scanner was set to scan from 10° to 80° with a scan rate of 1°/min. Raman spectra of the samples were measured using a Raman spectroscopy (Thermo scientific, with a laser wavelength of 785 nm) at a laser power of 0.2 mW and a magnification of 50×. The size and morphologies of the $Bi_4Ti_3O_{12}$ nanofibers were characterized using a scanning electron microscope (SEM, Hitachi S-4800). The nanostructures of the $Bi_4Ti_3O_{12}$ nanofibers and the Au-$Bi_4Ti_3O_{12}$ nanofibers were observed using transmission electron microscopy (TEM, Hitachi H-8100IV). Prior to the SEM observation, the electrodes were covered with a Au coating to improve their conductivity. The absorption spectra of the samples were obtained using a UV-vis near-infrared spectrophotometer (UV-3600, Shimadzu). X-ray photoelectron spectroscopy (XPS, Thermo ESCALAB 250) was performed with an Al target (15 kV, 10 mA) to determine the surface chemical composition of the samples.

3.4. Degradation of Ciprofloxacin

The piezo-photocatalytic behaviors of the $Bi_4Ti_3O_{12}$ nanofibers and the Au-$Bi_4Ti_3O_{12}$ nanofibers were measured by the decomposition of ciprofloxacin. The change in concentration of the ciprofloxacin was measured using a UV-Vis spectrophotometer. Moreover, the degradation effect was reflected by the change of absorbance. In typical conditions, a concentration of 20mg/L of ciprofloxacin solution (100 mL) and 50 mg of catalyst were

used during each experiment for every catalyst. Before testing the photocatalytic activity (under dark conditions), a reaction solution of ciprofloxacin and 50 mg catalyst was put into the beaker and stirred for 30 min using a magnetic stirrer to attain equilibrium (adsorption-desorption). The beaker was placed in a small ultrasonic machine (with ultrasonic power of 40 KHz) under a xenon lamp (300 W, light power 99.99 mW/cm^2). The experiment was conducted according to the requirements of using just the lamp (photocatalytic reaction), just the ultrasonic machine (piezoelectric reaction), or the lamp and ultrasonic machine together (piezo-photocatalytic reaction) as the experimental instruments. During the photocatalytic reactions, 1 mL solution was taken out of the reaction mixture every 10 min. Then the reaction mixture was centrifuged to remove traces of the catalyst.

3.5. Photoelectrochemistry Measurements

The photocurrent densities and electrochemical impedance spectroscopy of the $Bi_4Ti_3O_{12}$ nanofibers and the Au-$Bi_4Ti_3O_{12}$ nanofibers were tested using an electrochemical workstation (CHI760E, China). This workstation was equipped with a standard three-electrode system with a platinum plate, a saturated Ag/AgCl electrode, and obtained samples as the counter, reference, and working electrodes, respectively. The prepared samples were directly spread onto an indium tin oxide glass electrode to prepare the working electrodes, and a Na_2SO_4 (0.1 M, pH 7.0) aqueous solution was used as the electrolyte for the photocurrent measurements. The studied area of the thin films was fixed to 1 cm^2. The light source was supplied by a 300 W Xe arc lamp equipped with filter (AM 1.5 G) and with a power density of 100 mW cm^{-2}.

4. Conclusions

In summary, in order to obtain high efficiency in the photocatalytic degradation of antibiotics, Au-loaded ferroelectric $Bi_4Ti_3O_{12}$ nanofibers were obtained by electrospinning and ion sputtering. The characterization of the morphology, crystal structure and optical properties indicated that the $Bi_4Ti_3O_{12}$ nanofibers with orthorhombic crystal phases were prepared successfully. Furthermore, the degradation efficiency of ciprofloxacin by the $Bi_4Ti_3O_{12}$ nanofibers and the Au-$Bi_4Ti_3O_{12}$ nanofibers was investigated under light, with ultrasonic vibration and with both light and ultrasonic vibration. The results are as follows: In a 90 min reaction, 50% of the CIP was degraded with vibration only, and the reaction rate constant was 0.00809 min^{-1}. Under the condition of light only, 87.45% of the CIP was degraded, and the reaction rate constant was 0.02019 min^{-1}. Under both light and vibration, 100% of the CIP was degraded, and the reaction rate constant was 0.03141 min^{-1}, which is 0.01122 min^{-1} faster than that under light only. At the same time, after loading the Au, the catalytic performance was significantly enhanced under all three conditions. Under light and ultrasonic vibration, the CIP degradation efficiency of the Au-$Bi_4Ti_3O_{12}$ nanofibers reached 100% within 60 min, and the reaction rate constant was 0.06187 min^{-1}, which is twice as fast as the $Bi_4Ti_3O_{12}$ nanofibers. It is further observed that the photocurrent density was increased from 5.08×10^{-7} A/cm^2 to 8.17×10^{-6} A/cm^2. This work provides a basis for more research on the piezoelectric coupling effect in photocatalytic degradation and promotes the practical application of piezoelectric catalysis technology in the environmental field.

References

1. Guo, F.; Zhang, H.; Li, H.; Shen, Z.R. Modulating the oxidative active species by regulating the valence of palladium cocatalyst in photocatalytic degradation of ciprofloxacin. *Appl. Catal. B Environ.* **2022**, *306*, 121092. [CrossRef]
2. Hunge, Y.M.; Yadav, A.A.; Kang, S.W.; Lim, S.J.; Kim, H. Visible light activated MoS_2/ZnO composites for photocatalytic degradation of ciprofloxacin antibiotic and hydrogen production. *J. Photochem. Photobiol. A Chem.* **2023**, *434*, 114250. [CrossRef]
3. Lu, N.; Wang, P.; Su, Y.; Yu, H.T.; Liu, N.; Quan, X. Construction of Z-Scheme g-C_3N_4/RGO/WO_3 with in situ photoreduced graphene oxide as electron mediator for efficient photocatalytic degradation of ciprofloxacin. *Chemosphere* **2019**, *215*, 444–453. [CrossRef] [PubMed]
4. Xiong, Z.K.; Zhang, H.; Zhang, W.C.; Lai, B.; Yao, G. Removal of nitrophenols and their derivatives by chemical redox: A review. *Chem. Eng. J.* **2019**, *359*, 13–31. [CrossRef]
5. Hu, K.; Li, R.Q.; Ye, C.L.; Wang, A.Q.; Wei, W.Q.; Hu, D.; Qiu, R.L.; Yan, K. Facile synthesis of Z-scheme composite of TiO_2 nanorodig-C_3N_4 nanosheet efficient for photocatalytic degradation of ciprofloxacin. *J. Clean. Prod.* **2020**, *253*, 120055. [CrossRef]
6. Hoffmann, M.R.; Martin, S.T.; Choi, W.Y.; Bahnemann, D.W. Environmental applications of semiconductor photocatalysis. *Chem. Rev.* **1995**, *95*, 69–96. [CrossRef]
7. Meng, C.; Weng, B. Steric effects of a homogeneous $CuCl_2$/solvent system for photocatalytic selective oxidation of benzyl alcohol. *New J. Chem.* **2022**, *46*, 13345–13351. [CrossRef]
8. Tamaki, Y.; Furube, A.; Murai, M.; Hara, K.; Katoh, R.; Tachiya, M. Dynamics of efficient electron-hole separation in TiO_2 nanoparticles revealed by femtosecond transient absorption spectroscopy under the weak-excitation condition. *Phys. Chem. Chem. Phys.* **2007**, *9*, 1453–1460. [CrossRef]
9. Meng, C.; Yang, K.; Fu, X.Z.; Yuan, R.S. Photocatalytic Oxidation of Benzyl Alcohol by Homogeneous $CuCl_2$/Solvent: A Model System to Explore the Role of Molecular Oxygen. *ACS Catal.* **2015**, *5*, 3760–3766. [CrossRef]
10. Meng, C.; Wang, H.; Wu, Y.B.; Fu, X.Z.; Yuan, R.S. Study on Selective Photocatalytic Oxidation of Ethanol During TiO_2 Promoted Water-Splitting Process. *Acta Chim. Sin.* **2017**, *75*, 508–513. [CrossRef]
11. Huang, H.; Zhao, J.; Weng, B.; Lai, F.; Zhang, M.; Hofkens, J.; Roeffaers, M.B.J.; Steele, J.A.; Long, J. Site-Sensitive Selective $CO_{(2)}$ Photoreduction to CO over Gold Nanoparticles. *Angew. Chem. Int. Ed. Engl.* **2022**, *61*, e202204563. [PubMed]
12. Huang, H.; Verhaeghe, D.; Weng, B.; Ghosh, B.; Zhang, H.; Hofkens, J.; Steele, J.A.; Roeffaers, M.B.J. Metal Halide Perovskite Based Heterojunction Photocatalysts. *Angew. Chem. Int. Ed. Engl.* **2022**, *61*, e202203261. [PubMed]
13. Wang, H.; Hu, P.; Zhou, J.; Roeffaers, M.B.J.; Weng, B.; Wang, Y.; Ji, H. Ultrathin 2D/2D Ti_3C_2Tx/semiconductor dual-functional photocatalysts for simultaneous imine production and H_2 evolution. *J. Mater. Chem. A* **2021**, *9*, 19984–19993. [CrossRef]
14. Liu, S.; Qi, W.; Adimi, S.; Guo, H.; Weng, B.; Attfield, J.P.; Yang, M. Titanium Nitride-Supported Platinum with Metal-Support Interaction for Boosting Photocatalytic H(2) Evolution of Indium Sulfide. *ACS Appl. Mater. Interfaces* **2021**, *13*, 7238–7247. [CrossRef] [PubMed]
15. Long, Z.Q.; Li, Q.G.; Wei, T.; Zhang, G.M.; Ren, Z.J. Historical development and prospects of photocatalysts for pollutant removal in water. *J. Hazard. Mater.* **2020**, *395*, 122599. [CrossRef]
16. Luo, L.; Zhang, T.T.; Wang, M.; Yun, R.P.; Xiang, X. Recent Advances in Heterogeneous Photo-Driven Oxidation of Organic Molecules by Reactive Oxygen Species. *Chemsuschem* **2020**, *13*, 5173–5184. [CrossRef]
17. Nosaka, Y.; Nosaka, A.Y. Generation and Detection of Reactive Oxygen Species in Photocatalysis. *Chem. Rev.* **2017**, *117*, 11302–11336. [CrossRef]
18. Wang, Y.; Wen, X.R.; Jia, Y.M.; Huang, M.; Wang, F.F.; Zhang, X.H.; Bai, Y.Y.; Yuan, G.L.; Wang, Y.J. Piezo-catalysis for nondestructive tooth whitening. *Nat. Commun.* **2020**, *11*, 1328. [CrossRef]
19. Wang, S.S.; Wu, Z.; Chen, J.; Ma, J.P.; Ying, J.S.; Cui, S.C.; Yu, S.G.; Hu, Y.M.; Zhao, J.H.; Jia, Y.M. Lead-free sodium niobate nanowires with strong piezo-catalysis for dye wastewater degradation. *Ceram. Int.* **2019**, *45*, 11703–11708. [CrossRef]
20. Lan, S.Y.; Feng, J.X.; Xiong, Y.; Tian, S.H.; Liu, S.W.; Kong, L.J. Performance and Mechanism of Piezo-Catalytic Degradation of 4-Chlorophenol: Finding of Effective Piezo-Dechlorination. *Environ. Sci. Technol.* **2017**, *51*, 6560–6569. [CrossRef]
21. Xu, S.W.; Qian, W.Q.; Zhang, D.; Zhao, X.; Zhang, X.M.; Li, C.B.; Bowen, C.R.; Yang, Y. A coupled photo-piezo-catalytic effect in a BST-PDMS porous foam for enhanced dye wastewater degradation. *Nano Energy* **2020**, *77*, 105305. [CrossRef]
22. Yu, C.Y.; He, J.J.; Tan, M.X.; Hou, Y.X.; Zeng, H.; Liu, C.B.; Meng, H.M.; Su, Y.J.; Qiao, L.J.; Lookman, T.; et al. Selective Enhancement of Photo-Piezocatalytic Performance in $BaTiO_3$ Via heterovalent Ion Doping. *Adv. Funct. Mater.* **2022**, *32*, 2209365. [CrossRef]
23. Liu, Q.; Li, Z.Y.; Li, J.; Zhan, F.Q.; Zhai, D.; Sun, Q.W.; Xiao, Z.D.; Luo, H.; Zhang, D. Three dimensional $BaTiO_3$ piezoelectric ceramics coated with TiO_2 nanoarray for high performance of piezo-photoelectric catalysis. *Nano Energy* **2022**, *98*, 107267. [CrossRef]

24. Hervoches, C.H.; Lightfoot, P. A variable-temperature powder neutron diffraction study of ferroelectric $Bi_4Ti_3O_{12}$. *Chem. Mater.* **1999**, *11*, 3359–3364. [CrossRef]

25. Chen, Z.W.; Jiang, H.; Jin, W.L.; Shi, C.K. Enhanced photocatalytic performance over $Bi_4Ti_3O_{12}$ nanosheets with controllable size and exposed {001} facets for Rhodamine B degradation. *Appl. Catal. B Environ.* **2016**, *180*, 698–706. [CrossRef]

26. Liu, G.; Yang, H.G.; Pan, J.; Yang, Y.Q.; Lu, G.Q.; Cheng, H.M. Titanium Dioxide Crystals with Tailored Facets. *Chem. Rev.* **2014**, *114*, 9559–9612. [CrossRef]

27. Liu, X.T.; Shen, X.F.; Sa, B.S.; Zhang, Y.G.; Li, X.; Xue, H. Piezotronic-enhanced photocatalytic performance of heterostructured $BaTiO_3/SrTiO_3$ nanofibers. *Nano Energy* **2021**, *89*, 106391. [CrossRef]

28. Hu, J.Y.; Chen, Y.X.; Zhou, Y.Y.; Zeng, L.X.; Huang, Y.C.; Lan, S.Y.; Zhu, M.S. Piezo-enhanced charge carrier separation over plasmonic Au-BiOBr for piezo-photocatalytic carbamazepine removal. *Appl. Catal. B Environ.* **2022**, *311*, 121369. [CrossRef]

29. Zhang, Y.; Wang, S.; Zhao, Y.; Ding, Y.; Zhang, Z.; Jiang, T.; Wang, Z.L.; Li, L. Piezo-phototronic effect boosted catalysis in plasmonic bimetallic ZnO heterostructure with guided fermi level alignment. *Mater. Today Nano* **2022**, *18*, 100177. [CrossRef]

30. Fan, Z.X.; Zhu, Y.H.; Huang, X.; Han, Y.; Wang, Q.X.; Liu, Q.; Huang, Y.; Gan, C.L.; Zhang, H. Synthesis of Ultrathin Face-Centered-Cubic Au@Pt and Au@Pd Core-Shell Nanoplates from Hexagonal-Close-Packed Au Square Sheets. *Angew. Chem. Int. Ed.* **2015**, *54*, 5672–5676. [CrossRef]

31. Tatarchuk, T.; Myslin, M.; Mironyuk, I.; Bououdina, M.; Pedziwiatr, A.T.; Gargula, R.; Bogacz, B.F.; Kurzydlo, P. Synthesis, morphology, crystallite size and adsorption properties of nanostructured Mg-Zn ferrites with enhanced porous structure. *J. Alloy. Compd.* **2020**, *819*, 152945. [CrossRef]

32. Xie, Y.; Zhou, Y.P.; Gao, C.M.; Liu, L.J.; Zhang, Y.F.; Chen, Y.; Shao, Y. Construction of AgBr/BiOBr S-scheme heterojunction using ion exchange strategy for high-efficiency reduction of CO_2 to CO under visible light. *Sep. Purif. Technol.* **2022**, *303*, 122288. [CrossRef]

33. Li, B.S.; Lai, C.; Zhang, M.M.; Liu, S.Y.; Yi, H.; Liu, X.G.; An, N.; Zhou, X.R.; Li, L.; Fu, Y.K.; et al. N, S-GQDs and Au nanoparticles co-modified ultrathin Bi2MoO6 nanosheet with enhanced charge transport dynamics for full-spectrum-light-driven molecular oxygen activation. *Chem. Eng. J.* **2021**, *409*, 128281. [CrossRef]

34. You, D.T.; Wang, R.; Xie, J.W.; Liu, L.; Li, K.W.; Han, X.L.; Guo, T.; Xu, C.X. Synergistic SERS enhancement and in situ monitoring of photocatalytic reactions in a plasmonic metal/ferroelectric hybrid system by the light-induced pyroelectric effect. *J. Mater. Chem. A* **2022**, *10*, 14078–14089. [CrossRef]

35. Chen, X.D.; Zhang, H.; Ci, C.G.; Sun, W.W.; Wang, Y. Few-Layered Boronic Ester Based Covalent Organic Frameworks/Carbon Nanotube Composites for High-Performance K-Organic Batteries. *ACS Nano* **2019**, *13*, 3600–3607. [CrossRef]

36. Guo, W.X.; Sun, W.W.; Lv, L.P.; Kong, S.F.; Wang, Y. Microwave-Assisted Morphology Evolution of Fe-Based Metal-Organic Frameworks and Their Derived Fe_2O_3 Nanostructures for Li-Ion Storage. *ACS Nano* **2017**, *11*, 4198–4205. [CrossRef]

37. Cuevas, A.J.S.; Cabrera, C.B.P.; Aguilar, C.A.H.; Padilla-Martinez, I.I.; Thangarasu, P.; Contreras, E.F.V.; Alonzo, F.R.; Narayanan, J. Effect of the structural integrity on the size and porosity of gold-implanted mixed-metal oxide nanocomposites: Their influence on the photocatalytic degradation of thioanisole. *Dalton Trans.* **2022**, *51*, 17671–17687. [CrossRef]

38. You, D.T.; Liu, L.; Yang, Z.Y.; Xing, X.X.; Li, K.W.; Mai, W.J.; Guo, T.; Xiao, G.Z.; Xu, C.X. Polarization-induced internal electric field to manipulate piezo-photocatalytic and ferro-photoelectrochemical performance in bismuth ferrite nanofibers. *Nano Energy* **2022**, *93*, 106852. [CrossRef]

39. Amulya, M.A.S.; Nagaswarupa, H.P.; Kumar, M.R.A.; Ravikumar, C.R.; Prashantha, S.C.; Kusuma, K.B. Sonochemical synthesis of $NiFe_2O_4$ nanoparticles: Characterization and their photocatalytic and electrochemical applications. *Appl. Surf. Sci. Adv.* **2020**, *1*, 100023. [CrossRef]

40. Xu, S.Y.; Guo, L.M.; Sun, Q.J.; Wang, Z.L. Piezotronic Effect Enhanced Plasmonic Photocatalysis by $AuNPs/BaTiO_3$ Heterostructures. *Adv. Funct. Mater.* **2019**, *29*, 1808737. [CrossRef]